Non-peer reviewed **Fast Report** submitted to SEISMICA

A multiple asymmetric bilateral rupture sequence derived from the peculiar tele-seismic P-waves of the 2025 Myanmar earthquake

Naohiro Inoue [† 1], **Ryo Yamaguchi** [† 1], **Yuji Yagi** [* 2], **Ryo Okuwaki** [2], **Enescu Bogdan** [3,4], **Tira Tadapansawut** [5]

[1]Graduate School of Science and Technology, University of Tsukuba, Tennodai 1-1-1, Tsukuba, Ibaraki 305 – 8572, Japan, [2]Institute of Life and Environmental Sciences, University of Tsukuba, Tennodai 1-1-1, Tsukuba, Ibaraki 305 – 8572, Japan, [3]Department of Geophysics, Graduate School of Science, Kyoto University, Kitashirakawa, Oiwake-cho, Sakyo-ku, Kyoto 606-8502, Japan, [4]National Institute for Earth Physics, Calugareni str. 12, P.O. Box MG-2, 077125, Magurele-Bucharest, Ilfov, Romania, [5]College of Integrated Science and Technology, Rajamangala University of Technology Lanna, 128 Huay Kaew Road, Muang, Chiang Mai, 50300, Thailand

Author contributions: *Conceptualization*: Y. Yagi. *Methodology*: Y. Yagi. *Validation*: Y. Yagi, R. Okuwaki. *Formal Analysis*: N. Inoue, R. Yamaguchi, Y. Yagi. *Investigation*: N. Inoue, R. Yamaguchi, Y. Yagi, R. Okuwaki. *Resources*: N. Inoue, R. Yamaguchi, Y. Yagi, R. Okuwaki. *Writing - Original draft*: N., R. Yamaguchi, Y. Yagi, R. Okuwaki, E. Bogdan, T. Tadapansawut. *Writing - Review & Editing*: N. Inoue, R. Yamaguchi, Y. Yagi, R. Okuwaki, E. Bogdan, T. Tadapansawut. *Visualization*: R. Yamaguchi, Y. Yagi, R. Okuwaki. *Supervision*: Y. Yagi. *Project administration*: Y. Yagi. *Funding acquisition*: Y. Yagi, R. Okuwaki.

Abstract A large strike-slip earthquake occurred in central Myanmar on March 28, 2025. The aftershock distribution suggests that the rupture of the mainshock propagated mainly to the south. However, a large-amplitude phase lasting 20 s, followed by a short-period pulse-like phase, were observed at the stations on the north side of the source, while on the south side tremor-like phases with multiple peaks continued for 90 s. Using the potency density tensor inversion method, we explain the ”unusual” waveform signature of the Myanmar earthquake by a multiple, asymmetric bilateral rupture, involving boomerang-like back-rupture propagation and supershear.

บทคัดย่อ แผ่นดินไหวขนาดใหญ่ที่เกิดจากรอยเลื่อนแนวระนาบในประเทศพม่า ณ วันที่ 28 มีนาคม พ.ศ. 2568 แสดงการกระจายตัวของอาฟเตอร์ช็อกและชี้ให้เห็นทิศทางกระบวนการเกิดรอยแตกของแผ่นดินไปทางทิศใต้จากจุดกำเนิดแผ่นดินไหว อย่างไรก็ตามความผิดปกติของคลื่นไหวสะเทือนที่บันทึกจากสถานีวัดทางตอนเหนือของแหล่งกำเนิดแสดงคลื่นแอมปริจูดสูงในช่วงระยะเวลา 20 วินาทีแรกตามด้วยพัลส์คลื่นคาบสั้น ในขณะที่คลื่นที่วัดได้จากสถานีทางใต้ของจุดกำเนิดแสดงคลื่นแอมปริจูดสูงหลายจุดต่อเนื่องจนถึงวินาทีที่ 90 จากผลการวิเคราะห์กลไกการการเกิดรอยแตกของแผ่นดิน ณ ขณะเกิดแผ่นดินไหวด้วยวิธีการผกผันค่าความหนาแน่นเทนเซอร์สามารถอธิบายความผิดปกติของสัญญาณคลื่นแผ่นดินไหวโดยแผ่นดินไหวในพม่าครั้งนี้เกี่ยวข้องกับการแยกตัวแบบไม่สมมาตรไปทางทิศเหนือและทิศใต้ อีกทั้งยังเกี่ยวข้องกับทิศทางการแตกตัวแผ่นดินแบบย้อนกลับและการแตกตัวเหนือความเร็วเฉือนหรือที่เรียกว่าแผ่นดินไหวซุปเปอร์เชียร์

*Corresponding author: yagi-y@geol.tsukuba.ac.jp; †equally contributed author

要旨 2025 年 3 月 28 日ミャンマー中部で大地震が発生した。観測された遠地実体波 P 波は、震源北部に位置する観測点において大振幅かつ鋭いパルス状のシグナルが観測される一方で、震源南部に位置する観測点においては孤立するパルス状のシグナルは見えず、微動を想起させるスパイク状の複数のシグナルが 90 秒ほど続くなど、余震分布から予想される震源南方への破壊指向性とは相容れない特異な特徴をもつ。本研究は高自由度な震源過程解析手法であるポテンシー密度テンソルインバージョンを 2025 年ミャンマー地震の遠地実体波 P 波に適用し、ブーメランのような逆破壊伝播や超せん断破壊を含む複数の非対称なバイラテラルな破壊を組み合わせたモデルで、特異な遠地実体波 P 波の特徴を説明できることを明らかにした。

Non-technical summary On March 28, 2025, a large and devastating earthquake occurred in central Myanmar. We used globally observed seismic records to build the source process model of the large earthquake and reveal how the earthquake rupture evolved along the fault. We find that the earthquake ruptured a fault segment of 400 km length, in 80 s. Within the broad apparent southward fast rupture, the detailed rupture evolution was complex, being characterized by a series of discrete sub-events, involving bi-directional, southward and northward ruptures that migrated at fast speeds, partly faster than the seismic shear waves can travel. These findings are critical for our understanding of earthquake-rupture dynamics and assessing the associated earthquake hazard.

1 Introduction

On March 28, 2025, a moment magnitude (M_{W}) 7.7 earthquake occurred around 20 km west of Mandalay in Myanmar (Fig. 1a). According to the U. S. Geological Survey (USGS) (USGS, 2025), the epicenter is located at 21.996°N, 95.926°E and the aftershocks are distributed in an area spanning from 21.7°N to 23°N latitude (Fig. 1a), suggesting that the main rupture propagated to the south from the epicenter. In and around the possible source region, the right-lateral Sagaing fault extends for about 1200-km, from northern Myanmar to the Andaman Sea (Fitch, 1972; McCaffrey, 1992; Bertrand and Rangin, 2003; Socquet et al., 2006; Sloan et al., 2017; Lindsey et al., 2023) (Fig. 1a). The possible rupture area is located in the central part of the Sagaing fault, which has been considered as a seismic gap, being prone to host a large earthquake (Fadil et al., 2023; Hurukawa and Maung Maung, 2011; Tha Zin Htet Tin et al., 2022; Yang et al., 2024). The earthquake has severely affected Myanmar and surrounding areas, causing significant damage to the infrastructure and people (e.g., Witze, 2025).

As seen in the globally observed teleseismic records associated with the 2025 Myanmar earthquake, the polarity of the P-wave first motion is positive at observation stations on the north side of the epicenter and negative at stations on the south side of the epicenter (Fig. 1e), which is consistent with the strike-slip focal mechanism with a dip angle of 60° determined by the Global Centroid Moment Tensor (GCMT) Project (Fig. 1c) (Dziewonski et al., 1981; Ekström et al., 2012). At the observation stations on the north side, large-amplitude waves were observed for 20 s after the P-wave first arrival and short-period pulse-like waves were observed following the large-amplitude phase (Fig. 1e). At the observation stations on the south side, tremor-like phases with multiple peaks continued until about 90 seconds

after the P-wave first arrival. The aftershock distribution may suggest that the propagation of the mainshock rupture was southward (Fig. 1). However, it is notable that the high-amplitude pulse-like waveform is not clearly observed at the stations in the expected rupture direction but rather identified at the stations on the north side of the epicenter (Fig. 1). This simple yet peculiar observation hints at the difficulty in explaining the "unusual" teleseismic P-waves of the Myanmar earthquake only via a simplified seismic source model, and suggests the necessity of flexibly analyzing, with a high-degree-of-freedom, the seismic source process by allowing changes in the focal mechanism and rupture speed and direction, including possible back-rupture propagation and supershear (e.g., Hicks et al., 2020; Okuwaki et al., 2020) along the mainshock fault.

In recent years, based on the approach of Yagi and Fukahata (2011) who considers the modeling errors of the Green's function, the Potency Density Tensor Inversion (PDTI) method has been proposed (Shimizu et al., 2020; Yamashita et al., 2022b). Using the PDTI, we can estimate the detailed source model, including information on the fault geometry (Shimizu et al., 2020). The PDTI has been applied to many earthquakes in various tectonic settings and has proven effective in estimating complex source processes (e.g., Hicks et al., 2020; Yamashita et al., 2021; Yagi et al., 2023). In this Fast Report, we apply the PDTI to the teleseismic P-waves of the 2025 Myanmar earthquake and infer an irregular rupture process involving back-rupture and supershear-rupture propagation, which can explain the peculiarity of the observed waveforms.

2 Method, Data and Model setting

According to the PDTI method (Shimizu et al., 2020; Yamashita et al., 2022b), fault slip occurring on multiple faults is represented by the potency density tensor on an assumed model plane (Shimizu et al., 2020), and the potency tensor is expressed as the sum of five basis double couples according to Kikuchi and Kanamori (1991). Following the approach of Yagi and Fukahata (2011), PDTI incorporates the uncertainty of the Green's function into the data covariance matrix and evaluates the optimal value of the hyperparameters using Akaike's Bayesian Information Criterion (ABIC; e.g., Akaike, 1980; Sato et al., 2022), thereby achieving stable estimation even for a high-degree-of-freedom seismic source model without overfitting. PDTI is formulated using the properties of teleseismic P-waveforms, which have low spatial resolution but are sensitive to changes in focal mechanism solution (Shimizu et al., 2020). In this study, we used the latest version of the PDTI method that introduced the time-adaptive smoothing (Yamashita et al., 2022b).

We used the vertical component of the teleseismic P-waveforms downloaded from the SAGE Wilber 3 system. We selected 58 stations that have adequate azimuthal coverage of the source region and sufficiently high signal-to-noise ratios. We adapted the standard PDTI data processing procedure, which has been verified in previous studies (e.g., Yamashita et al., 2022a). After manually correcting the arrival time of the P-wave, the observed waveforms were converted into velocity waveforms and decimated to 0.7 s sampling. The theoretical Green's function was calculated at 0.1 s intervals following the method of Kikuchi and Kanamori (1991), with the 1-D structure of the ak135 model (Kennett et al., 1995; Montagner and Kennett, 1996). The mainshock epicentral coordinates determined by the USGS were used for the initial rupture point, with the hypocentral depth was set to 18 km, based on an initial analysis. An alternative hypocentral depth of 10 km (e.g., USGS, 2025) was also tested; it turns out that the mainshock hypocentral depth does not significantly affect the inversion solution (Figs. S2, S3).

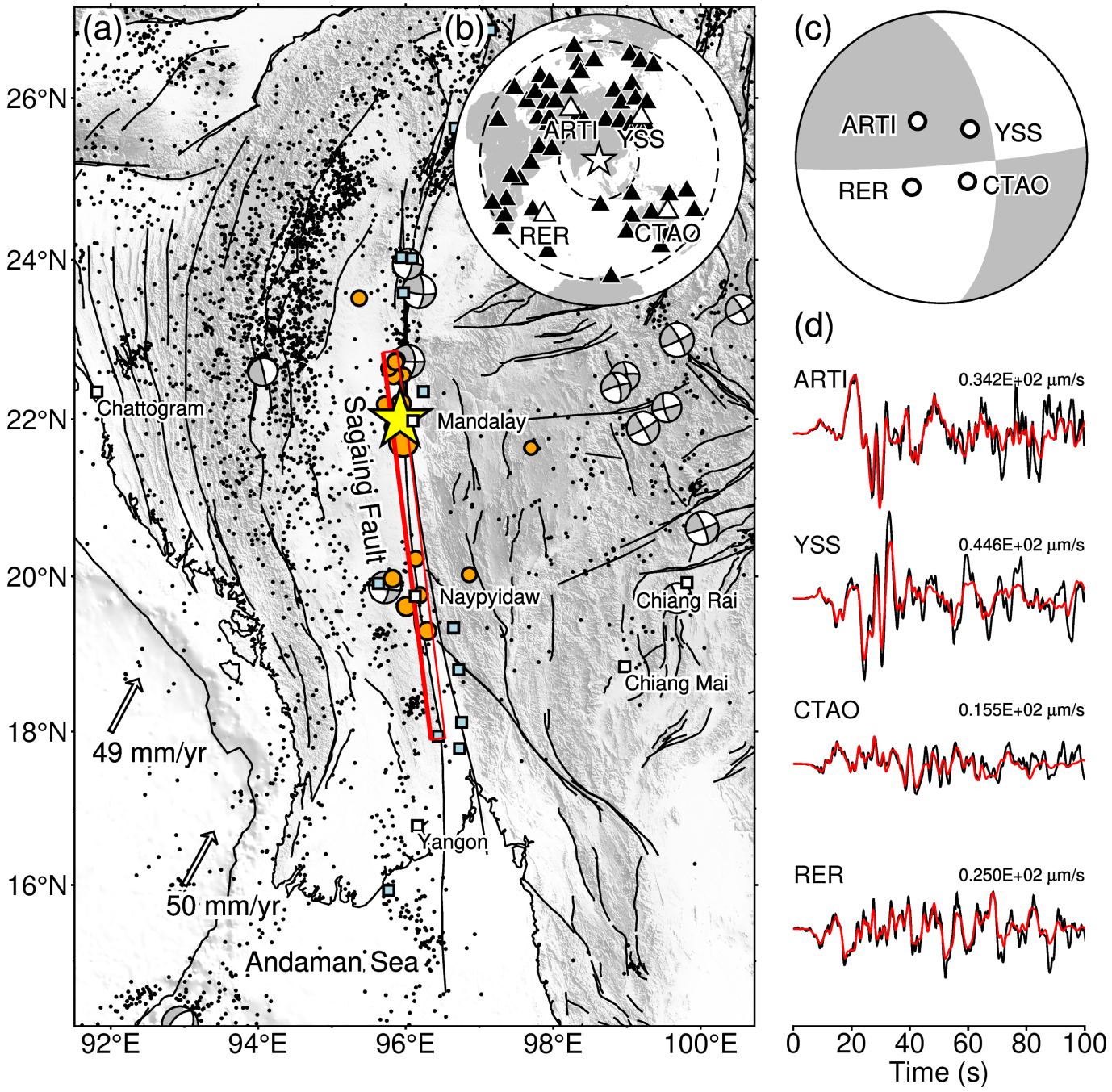

Figure 1 (a) Summary of the study region. The star and the orange circles show the mainshock epicenter and the three-day aftershocks (U.S. Geological Survey Earthquake Hazards Program, 2017; USGS, 2025), respectively. The blue square markers show the relocated earthquakes, including the historical events (Hurukawa and Maung Maung, 2011). The beachballs are the available GCMT solutions (Dziewonski et al., 1981; Ekström et al., 2012). The rectangle outlines the model plane used for our inversion with the thicker line representing the model top. The black lines are the active faults (Styron and Pagani, 2020). The arrows show relative plate motions (DeMets et al., 2010). The background topography is from SRTM15+V2 (Tozer et al., 2019). (b) The station distribution (triangles) used for our inversion. The dashed circles show epicentral distances of 30° and 90°. The star shows the epicenter. (c) The selected station locations on the lower hemisphere of the focal sphere of the GCMT solution (best double-couple) of the 2025 Myanmar earthquake. (d) Selected traces of the observed (black) and synthetic (red) waveforms. The corresponding stations are shown as white triangles in Fig. 1b. The maximum amplitude of the observed trace is on the right of each panel. All the traces used in our inversion are displayed in Fig. S1.

The strike and dip of the model plane were set to 353° and 60°, respectively, based on the GCMT solution. The length and width of the model plane were set to 468 km and 36 km, respectively. The knot spacing was set at 12 km in the strike direction and 5 km in the dip direction. The maximum duration of the potency-rate density function, for each space knot, was set to 49 s, and its sampling interval was set to 0.7 s. The total duration of the event was set to 90

s. The hypothetical maximum rupture front velocity was set at 6 km/s to be fast enough for allowing the possibility of supershear rupture. All of basis double-couple components were rotated so that the bset-fitting double-couple of the GCMT solution would become one of the basis double-couple components (e.g., Yagi et al., 2023).

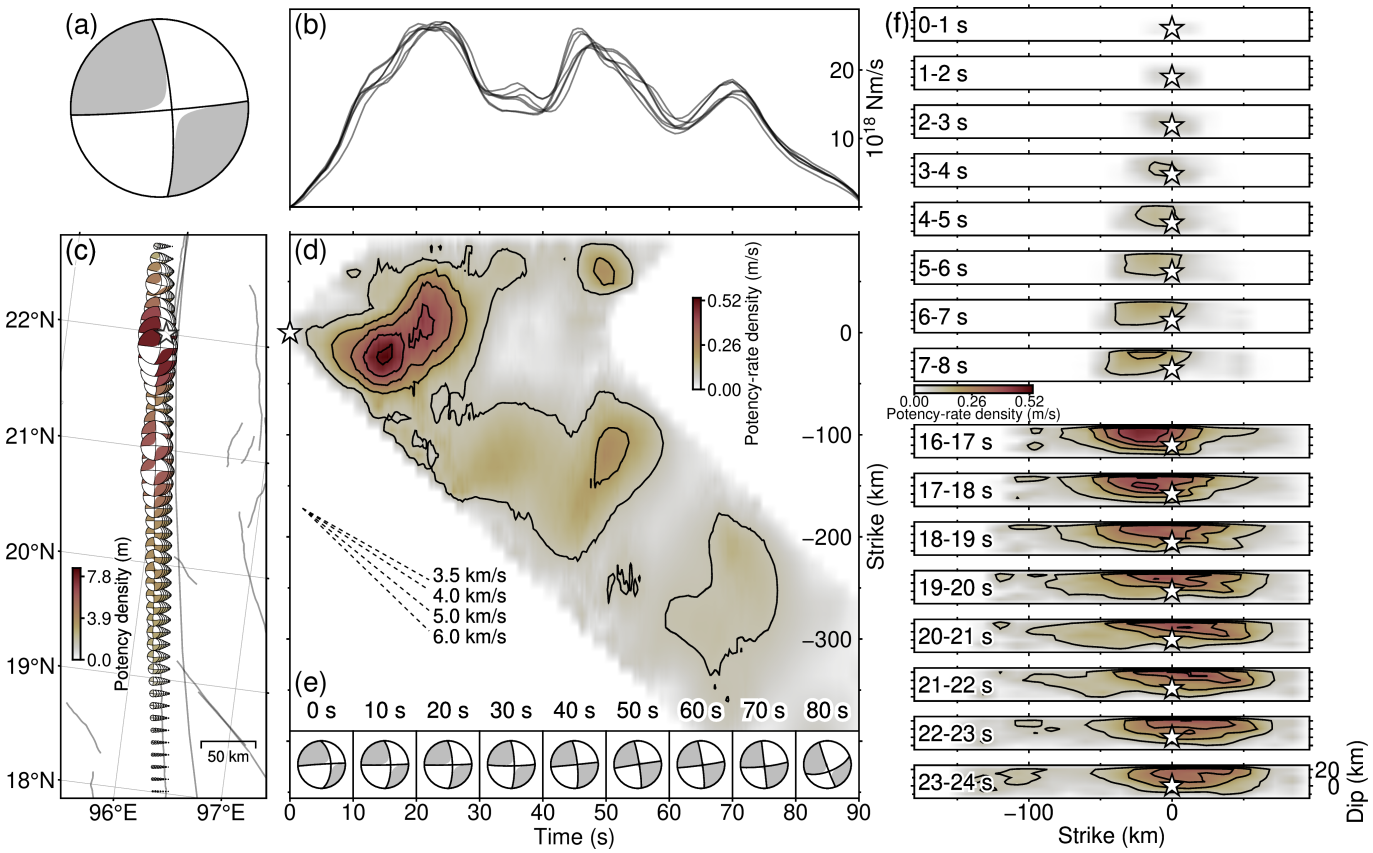

Figure 2 (a) The total moment tensor solution obtained by time-space integral of the potency-rate density tensors in a lower hemisphere projection. (b) The compilation of the moment-rate functions of the alternative models (Text S1). (c) The potency density tensor distribution obtained by time integral of the potency-rate density tensors. The star shows the initial rupture point. The lines show the active faults (Styron and Pagani, 2020). (d) The spatiotemporal evolution of the potency-rate density projected along the strike of the model plane. The contour interval is 0.1 m/s. The star shows the initial rupture point. Black dashed lines represent reference rupture speeds. (e) The snapshots of the moment tensor solution (lower hemisphere projection) of the averaged potency rate in the corresponding 10-s time window. The starting time of each window is shown at the top. (f) The snapshots of the potency-rate density distribution projected on the model plane. The white stars indicate the initial rupture point. The contour interval is 0.1 m/s. Only the domain around E1 of the model space is illustrated for the visibility of the figure.

3 Results

The resultant spatiotemporal distribution of the potency-rate density tensors shows multiple rupture episodes. We define at least three rupture episodes. The uncertainty and sensitivity of the solution to the different model settings are evaluated (Text S1 and Figs. S2, S3), and in the Results and Discussion sections we focus on the rupture features that are robustly resolved. The synthetic waveforms calculated from the estimated source process model reproduce the complex signatures of the observed waveforms, including the characteristic short-period pulse-like phase and the tremor-like phases with multiple peaks (Figs. 1d, S1).

The E1 episode: the initial rupture propagates from the hypocenter towards the south and shallow region, reaching the ground surface at 6 s from the origin time (OT), and reaching about 40 km south of the epicenter at OT+8 s (Figs. 2d and 2f). The main E1 rupture begins at OT+8 s, propagating asymmetrically, in a bilateral way, to the south and

north. The southern rupture reaches about 75 km south of the epicenter at OT+16 s, and becomes faint soon after that. The northern rupture propagates near surface, reaching about 65 km north of the epicenter at OT+20 s; the rupture fades from OT+25 s. The northern rupture area tends to be concentrated at shallow depths.

The E2 episode: from OT+24 s, another rupture episode begins around 120 km south of the hypocenter (Fig. 2d). It initially migrates towards both north and south directions, until OT+40 s. From OT+45 s to OT+58 s, the potency-rate density is relatively large throughout the E2 rupture region.

The E3 episode: although the potency-rate becomes relatively faint, and it gets difficult to rigorously infer obvious rupturing paths during OT+60–80 s, the rupture dominates the region of 200–400 km south from the epicenter, where it shows bilateral migration to the south and north (Fig. 2d).

The fault geometry can be inferred from our resultant potency-rate density tensors. We observe the progressive change of the fault geometry from north to south of the model domain (Fig. 2). The strike direction of the potency-rate density tensors shows counterclockwise rotation from 366° (or 6°) to 352° azimuth, from north to south of the model domain. The dip angle also changes. During E1, the dipping is shallow with an angle of 57° for the initial deep-to-shallow-southward rupture, and it gets steeper at 70° for the following dominant shallow northward rupture (Fig. 2e). The dip angle becomes steeper in the southern domain, reaching 80° during E2 and 87°–90° during E3 (Fig. 2e).

The potency density tensor distribution obtained by the time-integral of the potency-rate density tensors shows the two dominant peaks, centered at 10 km and 110 km south of the epicenter, which correspond to E1 and E2 (Figs. 2c, 2d). The total moment tensor solution obtained by time-space integration of the potency-rate density tensors is characterized by strike-slip faulting with a slight inclination of dip (79° for the north-south striking nodal plane) (Fig. 2a), and the seismic moment is 1.3×10^{21} N m (M_{W} 8.0).

4 Discussion and Conclusion

Although the broad rupture process of the 2025 Myanmar earthquake can be characterized by the southward rupture along the Sagaing fault, our study shows that it involves multiple, segmented rupture episodes, including asymmetric bilateral ruptures. We find at least three rupture episodes in our preferred solution. It is difficult to trace the rupture front propagating to the south, however, the estimated rupture migration velocity from the start time and location of E2 is about 4.6–5.4 km/s, which is faster than the S-wave velocity around the source region (Table S1). Both E1 and E2 exhibit a bilateral rupture that propagates both in north and south directions. Especially E1 favors the dominant northward rupture, where the northern wing of the bilateral rupture propagates at about 5 km/s, which is faster than S-wave velocity around the source region (Table S1). As shown in Fig. 1, the seismic records at observation stations on the north side of the epicenter show the large-amplitude phase followed by the sharp, impulsive signal in the earlier part of the traces (Fig. 1d). On the other hand, at observation stations on the south side, the teleseismic P-waves are characterized by tremor-like signatures with multiple peaks. The irregular, azimuthal dependence of the waveform signatures may not be explained by a simple unilateral southward rupture; the rupture rather involves a series of bilateral or boomerang-like backward ruptures and supershear ruptures towards north, as found in our PDTI solution.

An advantage of our PDTI method is the simultaneous estimation of fault rupture and geometry. As shown in Fig. 2, the resultant potency density tensors show the gradual, counterclockwise curvature of the strike orientation, which is consistent with the strike orientation of the Sagaing fault (e.g., Styron and Pagani, 2020). The spatial distribution of the dip angles also shows an along-strike variation from north to south of the epicenter: it shows shallow (around 60°–70° dip) dipping in the E1 region, which gets steeper (over 80° dip) in the E2 region. As shown by both the static potency distribution and the potency-rate distribution (Figs. 2c and 2d, respectively), the rupture domains of E1 and E2 are distinctly segmented. Such a segmentation can be robustly seen even if we adopt a different model setting (Figs. S2, S3). The segmentation of the rupture domains together with the spatial variation of the dip angles should characterize the possible along-strike heterogeneity of the Sagaing fault. Note, however, that our segmentation estimates rely on the inversion of teleseismic data, which has less spatial resolution compared to other datasets (e.g., SAR data).

The seismic moment obtained from the PDTI is 2.5 times larger than that of the GCMT solution. With other model settings, the seismic moment ranges from 1.27–1.34 $\times$ 10^{21} N m. This discrepancy between the seismic moment estimated by PDTI and a centroid moment tensor inversion may be due to a simplified seismic source model that is insufficient to represent the complex rupture process (Ohara et al., 2023). However, we should note that PDTI is designed to extract the details of the rupture process from the teleseismic P-waves and it does not target the accurate estimation of the seismic moment.

Due to the increase in the quality and quantity of teleseismic data, as well as development of data-driven analysis methods such as the PDTI, it has become possible to stably estimate seismic source processes that can reproduce peculiar observed waveforms like the ones of the 2025 Myanmar earthquake. As a result of applying the PDTI, the current study unearthed the complex seismic source process of the 2025 Myanmar earthquake, involving a series of bilateral or boomerang-like back-rupture propagation and supershear.

Acknowledgements

We thank the editor and reviewers for their thorough evaluation. This research is supported by Japan Society for the promotion of Science (JSPS) Grant-in-Aid for Scientific Research (C) 22K03751, JSPS Grant-in-Aid for Scientific Research (B) 25K01075 and JSPS Grant-in-Aid for Transformative Research Areas (A) “Science of Slow-to-Fast Earthquakes” 24H01020. The facilities of EarthScope Consortium were used for access to waveforms, related metadata, and/or derived products used in this study. These services are funded through the National Science Foundation’s Seismological Facility for the Advancement of Geoscience (SAGE) Award under Cooperative Agreement EAR-1724509. FPSPACK (Gasperini and Vannucci, 2003) software is used to handle the focal mechanisms obtained in the inversion. The ray parameter and travel-time are calculated with the TauP toolkit (Crotwell et al., 1999) for the theorical Green’s function. We used Generic Mapping Tools (v6.5.0; Wessels et al., 2019) and Scientific color maps (Crameri, 2018; Crameri et al., 2020) for data processing and visualization.

Data and code availability

The source code of the Potency Density Tensor Inversion is available at https://github.com/yujiyagi/pdti_public_version. The models presented in this paper are archived at https://doi.org/10.5281/zenodo.15190076. All seismic data were downloaded through the EarthScope Consortium Wilber 3 system (https://ds.iris.edu/wilber3/) including the following station networks: the G (GEOSCOPE; Institut De Physique Du Globe De Paris (IPGP) and Ecole Et Observatoire Des Sciences De La Terre De Strasbourg (EOST), 1982); the GT (GTSN; Albuquerque Seismological Laboratory (ASL)/USGS, 1993); the IC (NCDSN; Albuquerque Seismological Laboratory (ASL)/USGS, 1992); the II (IRIS/IDA - GSN; Scripps Institution of Oceanography, 1986); the IU (GSN - IRIS/USGS; Albuquerque Seismological Laboratory/USGS, 1988); and the MN (MedNet; MedNet Project Partner Institutions, 1990). The USGS events catalog is searched using https://earthquake.usgs.gov/earthquakes/search/ (U.S. Geological Survey Earthquake Hazards Program, 2017). The moment tensor solutions of the Global Centroid Moment Tensor (GCMT) catalog are available through https://www.globalcmt.org/CMTsearch.html (Dziewonski et al., 1981; Ekström et al., 2012). The ak135 (Kennett et al., 1995; Montagner and Kennett, 1996) and CRUST1.0 (Laske et al., 2013) are available through websites http://rses.anu.edu.au/seismology/ak135/ak135f.html and https://igppweb.ucsd.edu/~gabi/crust1.html, respectively. The active fault data is available at https://github.com/GEMScienceTools/gem-global-active-faults. Plate motion is calculated using Plate Motion Calculator (http://ofgs.aori.u-tokyo.ac.jp/~okino/platecalc_new.html). All figures were generated with Generic Mapping Tools (v6.5.0; https://docs.generic-mapping-tools.org/latest/index.html Wessels et al., 2019).

Competing interests

The authors have no competing interests.

References

Akaike, H. Likelihood and the Bayes procedure. *Trab. Estad. Y Investig. Oper.*, 31(1):143–166, 1980. doi: 10.1007/BF02888350.

Albuquerque Seismological Laboratory (ASL)/USGS. New China Digital Seismograph Network, 1992. doi: 10.7914/SN/IC.

Albuquerque Seismological Laboratory (ASL)/USGS. Global Telemetered Seismograph Network (USAF/USGS), 1993. doi: 10.7914/SN/GT.

Albuquerque Seismological Laboratory/USGS. Global Seismograph Network (GSN - IRIS/USGS), 1988. doi: 10.7914/SN/IU.

Bertrand, G. and Rangin, C. Tectonics of the western margin of the Shan plateau (central Myanmar): implication for the India – Indochina oblique convergence since the Oligocene. *Journal of Asian Earth Sciences*, 21(10):1139–1157, Aug. 2003. doi: 10.1016/S1367-9120(02)00183-9.

Crameri, F. Geodynamic diagnostics, scientific visualisation and StagLab 3.0. *Geosci. Model Dev.*, 11(6):2541–2562, 2018. doi: 10.5194/gmd-11-2541-2018.

Crameri, F., Shephard, G. E., and Heron, P. J. The misuse of colour in science communication. *Nat. Commun.*, 11(1):5444, 2020. doi: 10.1038/s41467-020-19160-7.

Crotwell, H. P., Owens, T. J., and Ritsema, J. The TauP Toolkit: Flexible Seismic Travel-time and Ray-path Utilities. *Seismological Research Letters*, 70(2):154–160, mar 1999. doi: 10.1785/gssrl.70.2.154.

DeMets, C., Gordon, R. G., and Argus, D. F. Geologically current plate motions. *Geophysical Journal International*, 181(1):1–80, apr 2010. doi: 10.1111/j.1365-246X.2009.04491.x.

Dziewonski, A. M., Chou, T.-A., and Woodhouse, J. H. Determination of earthquake source parameters from waveform data for studies of global and regional seismicity. *J. Geophys. Res. Solid Earth*, 86(B4):2825–2852, apr 1981. doi: 10.1029/JB086iB04p02825.

Ekström, G., Nettles, M., and Dziewoński, A. The global CMT project 2004 – 2010: Centroid-moment tensors for 13,017 earthquakes. *Phys. Earth Planet. Inter.*, 200-201:1–9, jun 2012. doi: 10.1016/j.pepi.2012.04.002.

Fadil, W., Wei, S., Bradley, K., Wang, Y., He, Y., Sandvol, E., Huang, B.-S., Hubbard, J., Thant, M., and Htwe, Y. M. M. Active Faults Revealed and New Constraints on Their Seismogenic Depth from a High-Resolution Regional Focal Mechanism Catalog in Myanmar (2016 – 2021). *Bulletin of the Seismological Society of America*, 113(2):613–635, Apr. 2023. doi: 10.1785/0120220195.

Fitch, T. J. Plate convergence, transcurrent faults, and internal deformation adjacent to Southeast Asia and the western Pacific. *J. Geophys. Res.*, 77(23):4432–4460, Aug. 1972. doi: 10.1029/JB077i023p04432.

Gasperini, P. and Vannucci, G. FPSPACK: a package of FORTRAN subroutines to manage earthquake focal mechanism data. *Comput. Geosci.*, 29(7):893–901, aug 2003. doi: 10.1016/S0098-3004(03)00096-7.

Hicks, S. P., Okuwaki, R., Steinberg, A., Rychert, C. A., Harmon, N., Abercrombie, R. E., Bogiatzis, P., Schlaphorst, D., Zahradnik, J., Kendall, J.-M., Yagi, Y., Shimizu, K., and Sudhaus, H. Back-propagating supershear rupture in the 2016 Mw 7.1 Romanche transform fault earthquake. *Nature Geoscience*, 13(9):647–653, sep 2020. doi: 10.1038/s41561-020-0619-9.

Hurukawa, N. and Maung Maung, P. Two seismic gaps on the Sagaing Fault, Myanmar, derived from relocation of historical earthquakes since 1918. *Geophysical Research Letters*, 38(1):L01310, jan 2011. doi: 10.1029/2010GL046099.

Institut De Physique Du Globe De Paris (IPGP) and Ecole Et Observatoire Des Sciences De La Terre De Strasbourg (EOST). GEOSCOPE, French Global Network of broad band seismic stations, 1982. doi: 10.18715/GEOSCOPE.G.

Kennett, B. L., Engdahl, E. R., and Buland, R. Constraints on seismic velocities in the Earth from traveltimes. *Geophys. J. Int.*, 122(1):108–124, 1995. doi: 10.1111/j.1365-246X.1995.tb03540.x.

Kikuchi, M. and Kanamori, H. Inversion of complex body waves-III. *Bull. Seism. Soc. Am.*, 81(6):2335–2350, 1991. doi: 10.1785/BSSA0810062335.

Laske, G., Masters, T. G., Ma, Z., and Pasyanos, M. Update on CRUST1.0 - A 1-degree Global Model of Earth's Crust. *https://igppweb.ucsd.edu/~gabi/crust1.html*, *Geophys. Res. Abstr. 15, Abstr. EGU2013-2658*, 15:Abstract EGU2013–2658, 2013.

Lindsey, E. O., Wang, Y., Aung, L. T., Chong, J.-H., Qiu, Q., Mallick, R., Feng, L., Aung, P. S., Tin, T. Z. H., Min, S. M., Bradley, K., Than, O., Oo, K. M., Thant, M., Masson, F., Bürgmann, R., and Hill, E. M. Active subduction and strain partitioning in western Myanmar revealed by a dense survey GNSS network. *Earth and Planetary Science Letters*, 622:118384, Nov. 2023. doi: 10.1016/j.epsl.2023.118384.

McCaffrey, R. Oblique plate convergence, slip vectors, and forearc deformation. *J. Geophys. Res.*, 97(B6):8905–8915, June 1992. doi: 10.1029/92JB00483.

MedNet Project Partner Institutions. Mediterranean Very Broadband Seismographic Network (MedNet), 1990. doi: 10.13127/SD/FBBBT-DTD6Q.

Montagner, J.-P. and Kennett, B. L. N. How to reconcile body-wave and normal-mode reference earth models. *Geophysical Journal International*, 125(1):229–248, apr 1996. doi: 10.1111/j.1365-246X.1996.tb06548.x.

Ohara, K., Yagi, Y., Yamashita, S., Okuwaki, R., Hirano, S., and Fukahata, Y. Complex evolution of the 2016 Kaikoura earthquake revealed by teleseismic body waves. *Progress in Earth and Planetary Science*, 10(1):35, jul 2023. doi: 10.1186/s40645-023-00565-z.

Okuwaki, R., Hirano, S., Yagi, Y., and Shimizu, K. Inchworm-like source evolution through a geometrically complex fault fueled persistent supershear rupture during the 2018 Palu Indonesia earthquake. *Earth and Planetary Science Letters*, 547:116449, oct 2020. doi: 10.1016/j.epsl.2020.116449.

Sato, D., Fukahata, Y., and Nozue, Y. Appropriate reduction of the posterior distribution in fully Bayesian inversions. *Geophys. J. Int.*, 231(2): 950–981, 2022. doi: 10.1093/gji/ggac231.

Scripps Institution of Oceanography. Global Seismograph Network - IRIS/IDA, 1986. doi: 10.7914/SN/II.

Shimizu, K., Yagi, Y., Okuwaki, R., and Fukahata, Y. Development of an inversion method to extract information on fault geometry from teleseismic data. *Geophysical Journal International*, 220(2):1055–1065, feb 2020. doi: 10.1093/gji/ggz496.

Sloan, R. A., Elliott, J. R., Searle, M. P., and Morley, C. K. Chapter 2 Active tectonics of Myanmar and the Andaman Sea. *Memoirs*, 48(1):19–52, Jan. 2017. doi: 10.1144/M48.2.

Socquet, A., Vigny, C., Chamot‐Rooke, N., Simons, W., Rangin, C., and Ambrosius, B. India and Sunda plates motion and deformation along their boundary in Myanmar determined by GPS. *J. Geophys. Res.*, 111(B5):2005JB003877, May 2006. doi: 10.1029/2005JB003877.

Styron, R. and Pagani, M. The GEM Global Active Faults Database. *Earthquake Spectra*, 36(1_suppl):160–180, oct 2020. doi: 10.1177/8755293020944182.

Tha Zin Htet Tin, Nishimura, T., Hashimoto, M., Lindsey, E. O., Aung, L. T., Min, S. M., and Thant, M. Present-day crustal deformation and slip rate along the southern Sagaing fault in Myanmar by GNSS observation. *Journal of Asian Earth Sciences*, 228:105125, May 2022. doi: 10.1016/j.jseaes.2022.105125.

Tozer, B., Sandwell, D. T., Smith, W. H. F., Olson, C., Beale, J. R., and Wessel, P. Global Bathymetry and Topography at 15 Arc Sec: SRTM15+. *Earth and Space Science*, 6(10):1847–1864, oct 2019. doi: 10.1029/2019EA000658.

U.S. Geological Survey Earthquake Hazards Program. Advanced National Seismic System (ANSS) Comprehensive Catalog of Earthquake Events and Products, 2017. doi: 10.5066/F7MS3QZH.

USGS. M 7.7 - 2025 Mandalay, Burma (Myanmar) Earthquake, 2025. https://earthquake.usgs.gov/earthquakes/eventpage/us7000pn9s/executive.

Wessels, R. J., Ellouz-Zimmermann, N., Bellahsen, N., Hamon, Y., Rosenberg, C., Deschamps, R., Momplaisir, R., Boisson, D., and Leroy, S. Polyphase tectonic history of the Southern Peninsula, Haiti: from folding-and-thrusting to transpressive strike-slip. *Tectonophysics*, 751: 125–149, 2019. doi: 10.1016/j.tecto.2018.12.011.

Witze, A. Deadly Myanmar earthquake was probably a rare rupture, scientists say. *Nature*, 640(8058):296–297, apr 2025. doi: 10.1038/d41586-025-00997-1.

Yagi, Y. and Fukahata, Y. Introduction of uncertainty of Green's function into waveform inversion for seismic source processes. *Geophysical Journal International*, 186(2):711–720, aug 2011. doi: 10.1111/j.1365-246X.2011.05043.x.

Yagi, Y., Okuwaki, R., Enescu, B., and Lu, J. Irregular rupture process of the 2022 Taitung, Taiwan, earthquake sequence. *Scientific Reports*, 13(1):1107, jan 2023. doi: 10.1038/s41598-023-27384-y.

Yamashita, S., Yagi, Y., Okuwaki, R., Shimizu, K., Agata, R., and Fukahata, Y. Consecutive ruptures on a complex conjugate fault system during the 2018 Gulf of Alaska earthquake. *Scientific Reports*, 11(1):5979, dec 2021. doi: 10.1038/s41598-021-85522-w.

Yamashita, S., Yagi, Y., and Okuwaki, R. Irregular rupture propagation and geometric fault complexities during the 2010 Mw 7.2 El Mayor-Cucapah earthquake. *Scientific Reports*, 12(1):4575, mar 2022a. doi: 10.1038/s41598-022-08671-6.

Yamashita, S., Yagi, Y., Okuwaki, R., Shimizu, K., Agata, R., and Fukahata, Y. Potency density tensor inversion of complex body waveforms with time-adaptive smoothing constraint. *Geophysical Journal International*, 231(1):91–107, jun 2022b. doi: 10.1093/gji/ggac181.

Yang, S., Xiao, Z., Wei, S., He, Y., Mon, C. T., Hou, G., Thant, M., Sein, K., and Jiang, M. New Insights Into Active Faults Revealed by a Deep‐Learning‐Based Earthquake Catalog in Central Myanmar. *Geophysical Research Letters*, 51(2):e2023GL105159, Jan. 2024. doi: 10.1029/2023GL105159.

Supplementary materials for

A multiple asymmetric bilateral rupture sequence derived from the peculiar tele-seismic P-waves of the 2025 Myanmar earthquake

Naohiro Inoue[1], Ryo Yamaguchi[1], Yuji Yagi[2], Ryo Okuwaki[2], Bogdan Enescu[3,4], and Tira Tadapansawut[5]

[1]Graduate School of Science and Technology, University of Tsukuba, Tennodai 1-1-1, Tsukuba, Ibaraki 305– 8572, Japan

[2]Institute of Life and Environmental Sciences, University of Tsukuba, Tennodai 1-1-1, Tsukuba, Ibaraki 305– 8572, Japan

[3]Department of Geophysics, Graduate School of Science, Kyoto University, Kitashirakawa, Oiwake-cho, Sakyo-ku, Kyoto 606-8502, Japan

[4]National Institute for Earth Physics, Calugareni str. 12, P.O. Box MG-2, 077125, Magurele-Bucharest, Ilfov, Romania

[5]College of Integrated Science and Technology, Rajamangala University of Technology Lanna, 128 Huay Kaew Road, Muang, Chiang Mai, 50300, Thailand

Contents:

Text S1

In this study, we introduced the uncertainty of the Green's function into the data covariance matrix, and estimated the hyperparameters using ABIC (Akaike, 1980), thereby achieving stable and detailed estimation of the seismic source process with a high-degree-of-freedom model (Yagi and Fukahata, 2011, Shimizu et al., 2020). However, our approach cannot evaluate the effect of non-Gaussian modeling errors resulting from the model settings. Here, we tested our modeling using multiple different model settings and evaluated the robustness of the results.

First, in order to evaluate the effect of the velocity structure setting on the inversion results, we used four velocity structures (Tables S2–S5) from CRUST1.0's 1x1-degree cells (Laske et al., 2013) around the seismic source region: the northeast model (cell center: 21.5°N, 96.5°E), the northwest model (cell center: 21.5°N, 95.5°E), southeast model (cell center: 20.5°N, 96.5°E) and southwest model (cell center: 20.5°N, 95.5°E). The other model settings were set at the same values as used for the optimum analysis. Fig. S2 shows the spatiotemporal evolution of the potency-rate density using different model settings. Using four different velocity structures it was found that the characteristics of E1 were well reproduced. For example, all models show that after the initial rupture propagated to the south, at 8 s from the origin time (OT) the rupture propagated asymmetrically in a bilateral way to the north and south. In addition, the characteristics of E2 were also reproduced, for example the feature showing the rupture started around 120 km south of the hypocenter, and propagated asymmetrically in a bilateral way to the south and north, as well as the feature showing the potency-rate density was relatively large throughout the E2 rupture region from OT+45 s to OT+58 s. When using the two velocity structures on the west side, the potency-rate density was high at the start of the rupture of the E2 episode. In addition, the estimates of the rupture area after OT+60 seconds tend to be sensitive to the velocity structure settings.

Next, in order to evaluate the effect of the model plane assumption on the inversion results, we performed an inversion with an alternative model plane inclination (dip angle) of 90° and an inversion with the hypocentral depth set to 10 km. Similar to the above structural model examination, the rupture propagation behavior of E1 and E2 were reproduced, but the characteristics of the potency rate distribution after OT+60 s varied depending on the model setting.

Finally, we set the knot interval of the potency-rate density function to 1.0 second and the input observed waveforms with a sampling interval of 1.0 s. In this case, the behavior of the rupture propagation in E1 and E2 were reproduced, but the rupture area after OT+60 seconds varied depending on the setting.

In summary, the examination using the seven alternative models considered in this study showed that the rupture propagation behavior in E1 and E2 were robustly estimated, while it was clear that the spatial distribution of the potency-rate density after OT+60 seconds could not be stably estimated.

Comparing the potency density tensor distributions on the map obtained by integrating the potency-rate density tensors (Fig. S3), it is confirmed that the areas with high potency density commonly exist from 21.5°N to 22.25°N and from 20.5°N to 21.25°N in all results. The strike direction of the potency density tensors shows the counterclockwise rotation from north to south of the model domain in all results. The feature that the dip of the north-south nodal plane is around 60° in the rupture area of E1 and around 80° in the rupture areas of E2 and E3 is reproduced even with different model settings. These results show that the potency density tensors distribution and the change of dip angle along strike direction are robustly reproduced.

Table S1: Structure from AK135-F (Kennett et al., 1995; Montagner and Kennett, 1996) used for calculating Green's functions

V_P (km/s)	V_S (km/s)	Density (10^3 kg/m^3)	Thickness (km)
5.80	3.46	2.45	20.00
6.50	3.85	2.71	15.00
8.04	4.48	3.30	- (Moho)

Table S2: The northeast structure model (cell center: 21.5°N, 96.5°E) from CRUST1.0 (Laske et al., 2013) used for calculating Green's functions

V_P (km/s)	V_S (km/s)	Density (10^3 kg/m^3)	Thickness (km)
6.10	3.55	2.74	14.80
6.30	3.65	2.78	13.61
7.00	3.99	2.95	5.93
8.01	4.45	3.30	- (Moho)

Table S3: The northwest structure model (cell center: 21.5°N, 95.5°E) from CRUST1.0 (Laske et al., 2013) used for calculating Green's functions

V_P (km/s)	V_S (km/s)	Density (10^3 kg/m^3)	Thickness (km)
2.50	1.07	2.11	0.34
4.00	2.13	2.37	4.00
5.00	2.88	2.54	1.00
5.90	3.44	2.67	10.04
6.30	3.62	2.74	9.73
6.90	3.87	2.91	9.73
8.06	4.48	3.32	- (Moho)

Table S4: The southeast structure model (cell center: 20.5°N, 96.5°E) from CRUST1.0 (Laske et al., 2013) used for calculating Green's functions

V_P (km/s)	V_S (km/s)	Density (10^3 kg/m^3)	Thickness (km)
6.10	3.55	2.74	14.65
6.30	3.65	2.78	13.61
7.00	3.99	2.95	5.94
7.96	4.43	3.28	- (Moho)

Table S5: The southwest structure model (cell center: 20.5°N, 95.5°E) from CRUST1.0 (Laske et al., 2013) used for calculating Green's functions

V_P (km/s)	V_S (km/s)	Density (10^3 kg/m^3)	Thickness (km)
2.50	1.07	2.11	0.23
4.00	2.13	2.37	4.00
5.00	2.88	2.54	2.50
5.90	3.44	2.67	9.52
6.30	3.62	2.74	9.24
6.90	3.87	2.91	9.24
8.02	4.46	3.31	- (Moho)

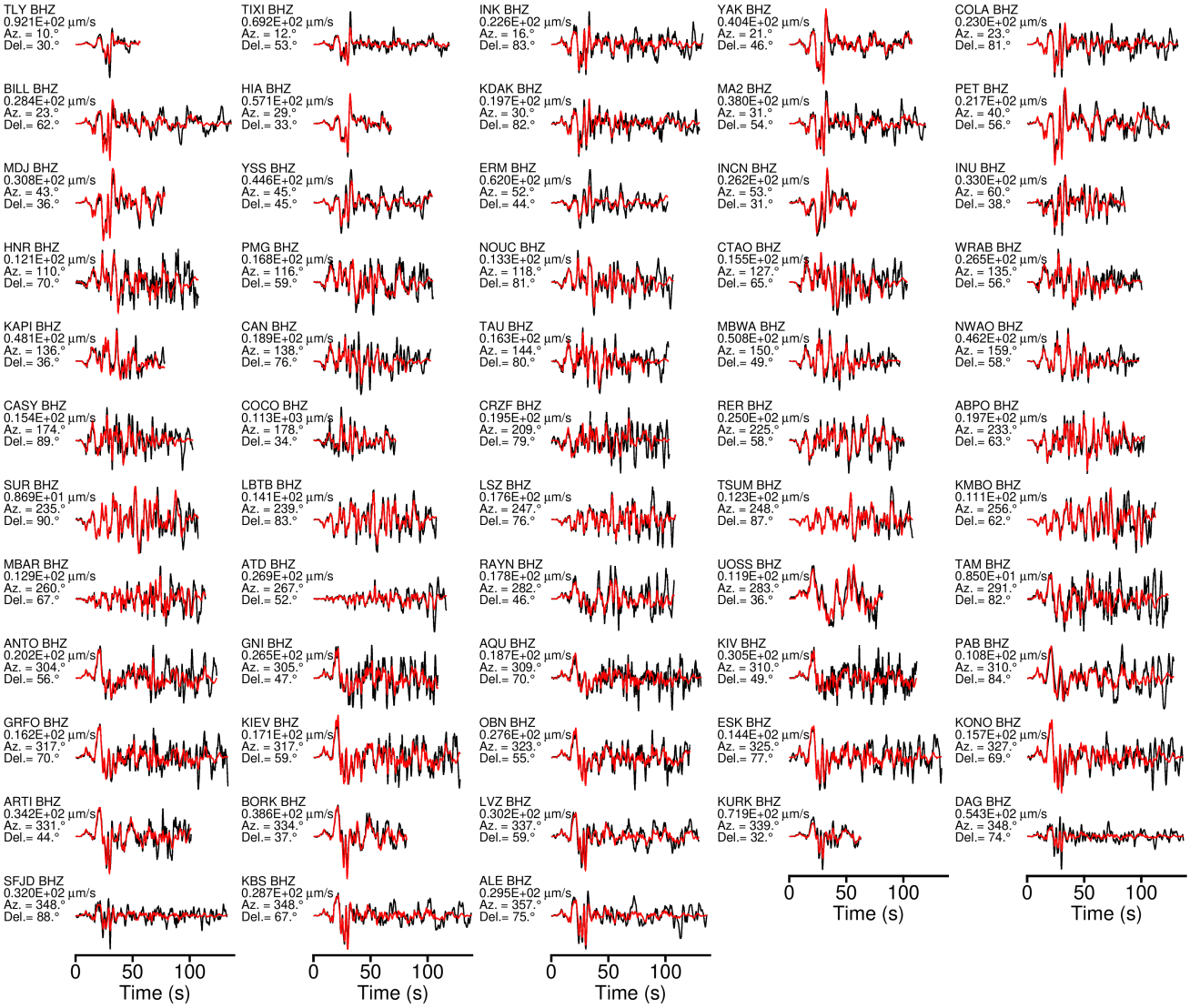

Figure S1. Observed (black) and synthetic (red) waveforms calculated from the optimum model. The station code and channel, maximum amplitude of observed data, station azimuth (Az.) and epicentral distance (Del.) are on the left of each panel.

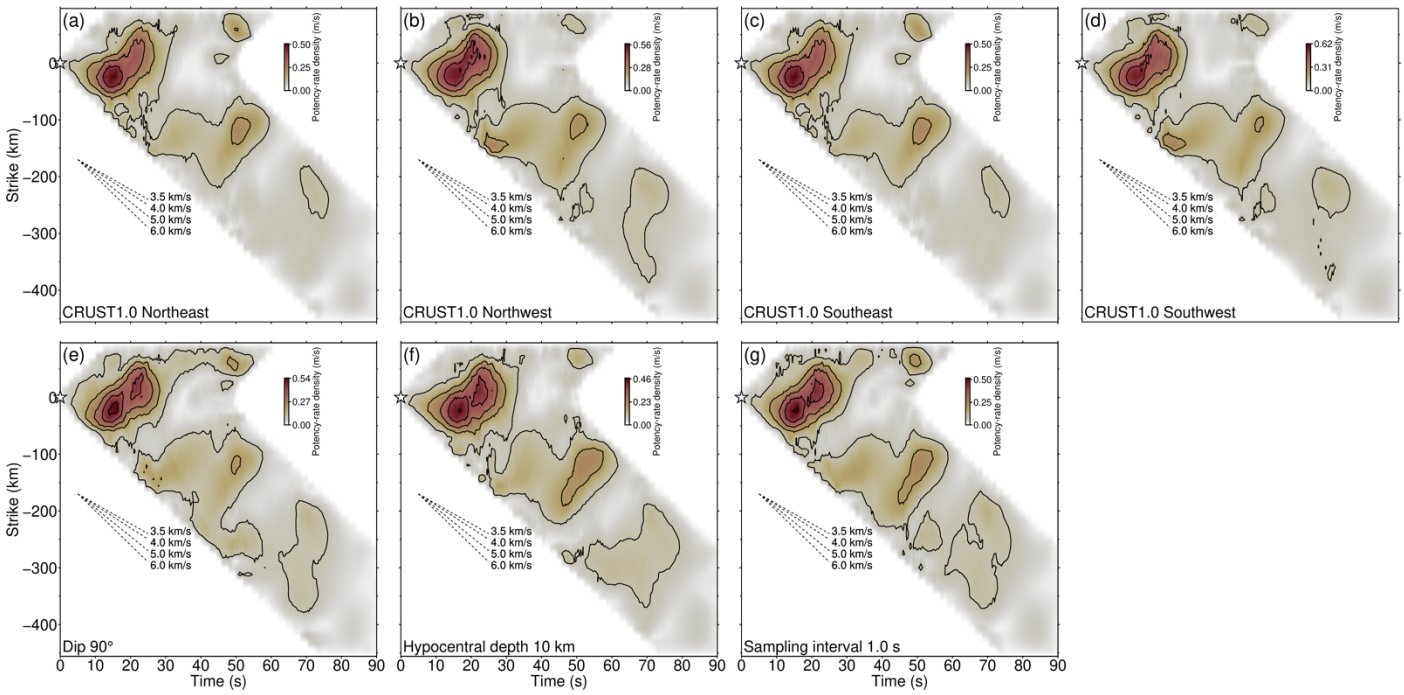

Figure S2. Compilation of potency-rate density evolution from the sensitivity test (Text S1). The star shows the initial rupture point. The dashed lines are the reference rupture speeds. (a–d) The solutions using the alternative structural models (Tables S2–S5). (e) The solution using the alternative model plane setting (90° dip). (f) The solution using the alternative initial rupture depth (10 km). (g) The solution using the alternative sampling interval (1.0 s).

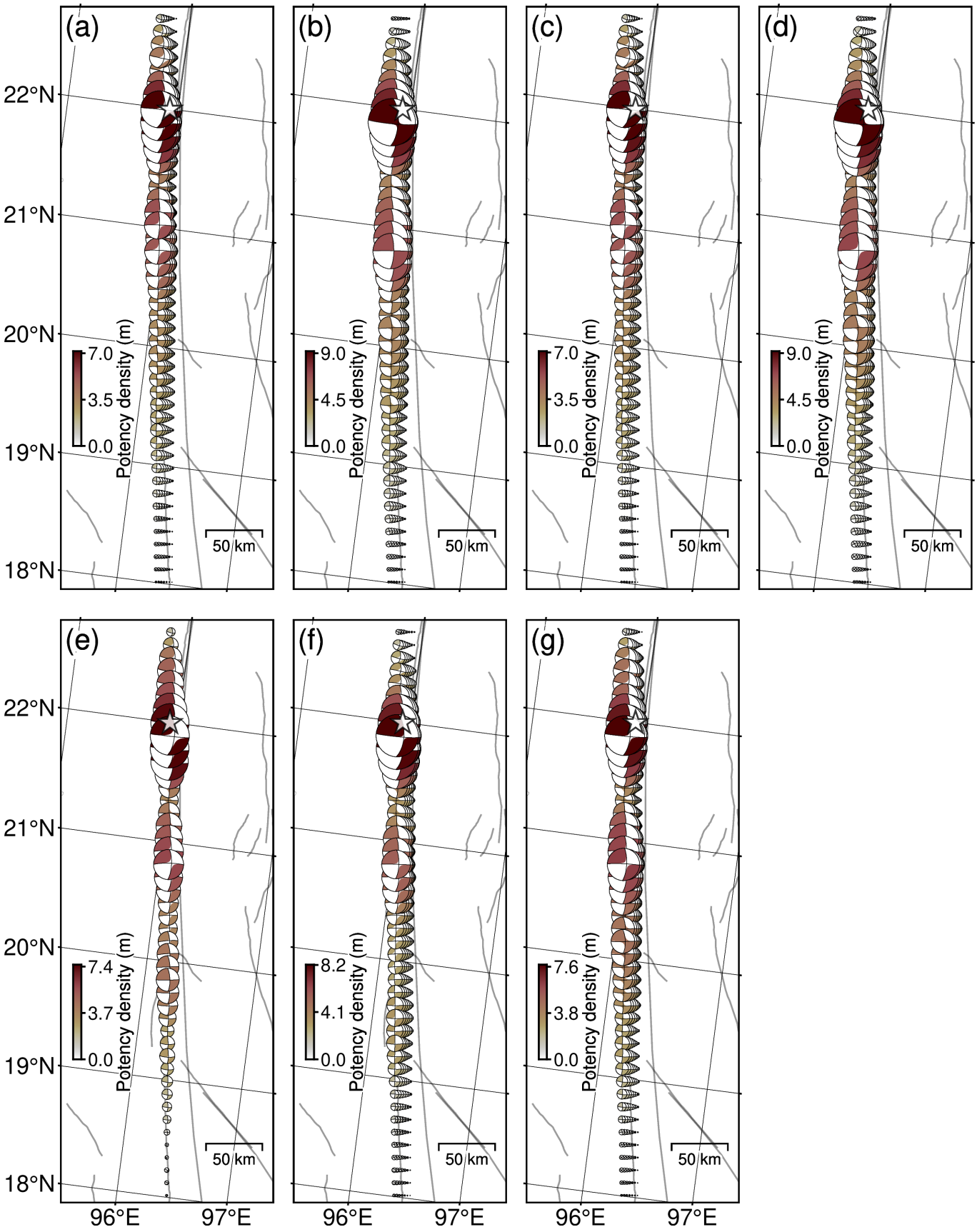

Figure S3. Compilation of potency density tensor distributions from the sensitivity test (Text S1). The star shows the initial rupture point. The lines show the active faults (Styron and Pagani, 2020). (a–d) The solutions using the alternative structural models (Tables S2–S5). (e) The solution using the alternative model plane setting (90° dip). (f) The solution using the alternative initial rupture depth (10 km). (g) The solution using the alternative sampling interval (1.0 s).

References

Akaike, H., 1980. Likelihood and the Bayes procedure. Trabajos de Estadistica Y de Investigacion Operativa, 31(1), 143–166. https://doi.org/10.1007/BF02888350

Kennett, B.L.N., Engdahl, E.R., Buland, R., 1995. Constraints on seismic velocities in the Earth from traveltimes. Geophysical Journal International 122, 108–124. https://doi.org/10.1111/j.1365-246X.1995.tb03540.x

Laske, G., Masters, G., Ma, Z., Pasyanos, M., 2013. Update on CRUST1.0 - A 1-degree Global Model of Earth's Crust EGU2013-2658.

Montagner, J.-P., Kennett, B.L.N., 1996. How to reconcile body-wave and normal-mode reference earth models. Geophysical Journal International 125, 229–248. https://doi.org/10.1111/j.1365-246X.1996.tb06548.x

Shimizu, K., Yagi, Y., Okuwaki, R., Fukahata, Y., 2020. Development of an inversion method to extract information on fault geometry from teleseismic data. Geophysical Journal International 220, 1055–1065. https://doi.org/10.1093/gji/ggz496

Styron, R., Pagani, M., 2020. The GEM Global Active Faults Database. Earthquake Spectra 36, 160–180. https://doi.org/10.1177/8755293020944182

Yagi, Y., Fukahata, Y., 2011. Introduction of uncertainty of Green's function into waveform inversion for seismic source processes: Uncertainty of Green's function in inversion. Geophysical Journal International 186, 711–720. https://doi.org/10.1111/j.1365-246X.2011.05043.x